Attribution of Chemistry-Climate Model Initiative (CCMI) ozone radiative flux bias from satellites

Le Kuai[1,2], Kevin W. Bowman[1,2], Helen Worden[3], Kazuyuki Miyazaki[2,4], Susan Kulawik[5], Andrew Conley[3], Jean-François Lamarque[3], Fabien Paulot[3], David Paynter[6], Luke D. Oman[7], Sarah Strode[8], Eugene Rozanov[9], Andrea Stenke[10], Laura Revell[11], David A. Plummer[12], Makoto Deushi[13], Patrick Jöckel[14], Markus Kunze[15]

1. Joint Institute For Regional Earth System Science and Engineering, University of California, Los Angeles, USA;
2. Jet Propulsion Laboratory, California Institute of Technology, USA;
3. National Center for Atmospheric Research, USA;
4. Japan Agency for Marine-Earth Science and Technology
5. Bay Area Environmental Research Institute, USA;
6. NOAA, Geophysical Fluid Dynamics Laboratory, USA;
7. NASA Goddard Space Flight Center, USA;
8. USRA, NASA Goddard Space Flight Center, USA;
9. Physikalisch-Meteorologisches Observatorium Davos– World Radiation Center (PMOD/WRC), Davos, Switzerland;
10. Institute for Atmospheric and Climate Science, ETH Zürich (ETHZ), Zürich, Switzerland;
11. School of Physical and Chemical Sciences, University of Canterbury, Christchurch, New Zealand;
12. Climate Research Branch, Environment and Climate Change Canada, Montreal, Canada;
13. Meteorological Research Institute, Japan;
14. Deutsches Zentrum für Luft- und Raumfahrt (DLR), Institut für Physik der Atmosphäre, Oberpfaffenhofen, Germany;
15. Freie Universität Berlin, Berlin, Germany

Correspondence to: Le Kuai (lkuai@jpl.nasa.gov)

Abstract

The top-of-atmosphere (TOA) outgoing longwave flux over the 9.6-µm ozone band is a fundamental quantity for understanding chemistry-climate coupling. However, observed TOA fluxes are hard to estimate as they exhibit considerable variability in space and time that depend on the distributions of clouds, ozone (O_3), water vapor (H_2O), air temperature (T_a), and surface temperature (T_s). Benchmarking present day fluxes and quantifying the relative influence of their drivers is the first step for estimating climate feedbacks from ozone radiative forcing and predicting its evolution.

To that end, we construct observational instantaneous radiative kernels (IRKs) representing the sensitivities of the TOA flux in the 9.6-µm ozone band to the vertical distribution of geophysical variables, including O_3, H_2O, T_a, and T_s based upon the Aura Tropospheric Emission Spectrometer (TES) measurements. Applying these kernels to present-day simulations from the

Chemistry-Climate Model Initiative (CCMI) project as compared to a 2006 reanalysis assimilating satellite observations, we show that the models have large differences in TOA flux, attributable to different geophysical variables. In particular, model simulations continue to diverge from observations in the tropics, as reported in previous studies of the Atmospheric

5 Chemistry Climate Model Inter-comparison Project (ACCMIP) simulations. The principal culprits are tropical mid and upper tropospheric ozone followed by tropical lower tropospheric H_2O. Five models out of the eight studied here have TOA flux biases exceeding 100 mWm^{-2} attributable to tropospheric ozone bias. Another set of five models flux biases over 50 mWm^{-2} due to H_2O. On the other hand, T_a radiative bias is negligible in all models (no more than 30

10 mWm^{-2}). We found that AM3 and CMAM have the lowest TOA flux biases globally but are a result of cancellation of difference processes. Overall, the multi-model ensemble mean bias is − 132.9±98 mWm^{-2}, indicating that they are too atmospherically opaque thereby reducing sensitivity of TOA flux to ozone and potentially an underestimate of ozone radiative forcing. We find that the inter-model TOA OLR difference is well anti-correlated with their ozone band

15 flux bias. This suggests that there is significant radiative compensation in the calculation of model outgoing longwave radiation.

1. Introduction

20 Tropospheric ozone (O_3) is the third important anthropogenic greenhouse gas (GHG) in terms of radiative forcing (RF) as a consequence of O_3 precursor and methane (CH_4) emission increases since pre-industrial to present day. Tropospheric O_3 RF ranges widely from +0.2 to +0.6 Wm^{-2} computed from chemistry-climate model ensembles (IPCC AR5, 2013) (Bowman, et al., 2013;Stevenson, et al., 2013). The large uncertainty of the tropospheric O_3 RF is driven in part

25 by the model responses to climate change. Without a good long-term record of the historical O_3 levels (Young, et al., 2017;Gaudel, et al., 2018), such estimates are highly dependent on the model assumptions of past O_3 levels. Differences between models in physical climate, chemical, and radiative processes conspire to complicate the assessment of the accuracy of these RF calculations. Consequently, a method to disentangle the key players caused the model

30 differences to observations as well as the difference between the models is critical to robust estimates of chemistry-climate coupling.

About 80% of tropospheric O_3 RF is due to O_3 longwave absorption with the remaining 20% from the shortwave absorption (IPCC AR5, 2013). In the longwave, 97% of the total longwave

35 absorption is in the 9.6-μm O_3 band (Rothman, et al., 1987). The global outgoing longwave radiation (OLR) spectra were first observed from space for a few months in 1970. Radiance observations were taken during April 1970 and January 1971 by NASA Infrared Interferometeric Spectrometer (IRIS) and then from October 1997 for 9 month by the Interferometeric Monitor of Greenhouse Gases (IMG) instrument, on board the Japanese Advanced Earth Observing

40 Satellite "Midori" (ADEOS) satellite. Harries, et al. (2001) showed that the changes in the greenhouse gas features between the observed spectra taken 30 years apart by these two instruments suggest increases in greenhouse gas forcing. Over the last two decades, a new generation of thermal infrared satellite instruments now provide a unique opportunity to continuously monitor the outgoing radiances covering the 9.6-μm O_3 band globally since 2002,

Atmospheric
Chemistry
and Physics
Discussions

such as NASA's tropospheric Emission Spectrometer (TES) and Atmospheric Infrared Sounder (AIRS), ESA's Infrared Atmospheric Sounding Interferometer (IASI), and NOAA's Cross-track Infrared Sounder (CrIS). These valuable long-term global measurements can be used to derive the top-of-atmosphere (TOA) O_3 band flux and the sensitivity of the flux to the vertical distributions of O_3, defined as instantaneous radiative kernels (IRKs) (Worden, et al., 2011;Doniki, et al., 2015).

The TES observed global TOA outgoing fluxes at the 9.6-μm O_3 band in clear sky (Fig. 1) show strong geographic variations as a result of the short life-time of O_3 (Worden et al., 2011; Bowman et al., 2013). Consequently, the global O_3 GHG effect is more unevenly distributed than long-lived GHG, such as CO_2. In addition, the variations of the TOA fluxes are not only highly dependent on the distributions of O_3, but are also dependent on water vapor (H_2O), air temperature (T_a), and surface temperature (T_s) (Kuai et al., 2017).

There is an additional factor where the large-scale atmospheric structure sets the overall atmospheric opacity, which describes the fraction of the light that fails to pass through the atmosphere due to the absorption or scattering. Changes in O_3 in more opaque regions, e.g., Western Pacific, result in a much smaller change in TOA flux than in more transparent regions, e.g., Middle East (Kuai, et al., 2017). This opacity has a direct impact on radiative forcing calculations.

Chemistry-climate models diverge significantly in the simulation of these processes, which are difficult to disentangle because it is hard to quantify the response of the TOA flux due to the atmospheric opacity. In this study, we introduce a method to use observational based IRKs to quantitatively estimate the contributions of the model biases in O_3, H_2O, T_a and T_s to the TOA flux biases. In addition, the presence of clouds is the primary control on atmospheric opacity. Under those conditions, the role of these other variables on TOA flux is less important. Consequently, we focus on clear sky conditions to quantify the role of O_3, H_2O, T_a and T_s in the variation of the TOA flux.

Worden et al, 2008 first attempted to disentangle these effects from satellites. They subsequently developed the instantaneous Radiative Kernel (IRK) in Worden et al, (2011) for O_3, which is used in this study as a powerful tool to attribute model variability. IRKs for O_3 represent the sensitivity of TOA fluxes to the vertical distributions of the observed O_3. Aghedo, et al. (2011) applied the TES IRKs to evaluated the O_3 radiative effect of chemistry-climate models' O_3 biases in the Atmospheric Chemistry Climate Model Inter-comparison project (ACCMIP) (Lamarque, et al., 2013). Bowman et al. (2013) found model OLR bias due to O_3 is correlated with RF in the ACCMIP models. This correlation was help to reduce the inter-model divergence in RF by about 30% (Myhre, et al., 2013). Doniki et al. (2015), updated the IRKs' calculation with a more accurate, but computationally more complicate method, a five Gaussian Integration (GI) method, to replace the anisotropic approximation. They computed the O_3 IRKs with IASI observations and also showed that between the two methods there are about 20% differences in IRKs and about 20-25% differences in the Longwave Radiative Effect (LWRE). They also found that the day and night difference of LWRE is mainly controlled by the T_s change instead of O_3

Atmospheric
Chemistry
and Physics
Discussions

Open Access

EGU

amount change. Kuai et al., (2017) updated the computational method for the TES O_3 IRK product with the five GI method and revealed the hydrological controls on the global distribution of the O_3 GHG effect. The study showed that H_2O, T_a and T_s affect the O_3 IRK strength through relative humidity.

5

Therefore, the TOA flux in the 9.6 micron band depends on more than O_3. Consequently, in this study we expand the TES observation-based IRKs to other quantities, including H_2O profiles, T_a profiles, and T_a. We apply these IRKs to help attribute the reasons for the model divergence in the TOA flux.

10

The questions that have never been answered before including 1) How do the model-based flux and the flux sensitivity compare to the observational-based flux and sensitivity? 2) How do they compare between the models? 3) How do the flux biases in models relate to the RF variation? Thus, benchmarking present day O_3 band flux is the first step to answer all these questions, and would help to further understand the correlations between the bias in TOA flux and the bias in

15   O_3 RF, and eventually improve the estimation of the climate feedbacks from O_3 forcing.

To benchmark the model simulated geophysical quantities, a recently developed multi-species multi-satellite Tropospheric Chemistry Reanalysis (TCR) product (Miyazaki, et al., 2015) is used

20   in this study to compare to the model results. This chemical reanalysis assimilates data from multiple satellites with sensitivity over complementary parts of the atmosphere, which provides better information than single-species chemical data assimilation. Satellite observations have the occasional issue of temporal discontinuity due to instrument performance and irregular spatial coverage, which can be circumvented by chemical data assimilation. Miyazaki et al.,

25   (2015) showed statistically the model error against independent aircraft and ozonesonde observations in the assimilated species, e.g. O_3, NO_2, and CO, is significantly reduced. The multi-species assimilation improves the Northern/Southern Hemisphere OH ratio and provides the emission estimates with interannual variation. The comparison of O_3 reanalysis to the ACCMIP ensemble O_3 simulation in Miyazaki and Bowman (2017) quantified the model discrepancies in

30   terms of seasonal amplitude, spatial variability, and inter-hemispheric gradient. For example, the ensemble mean is 6-11 ppb too high in the northern extra tropics, while up to 18 ppb too low in the southern tropics over the Atlantic in the lower troposphere. In this study, we use the same O_3 reanalysis data (Miyazaki and Bowman, 2017) to understand the model bias in the Chemistry-Climate Model Initiative (CCMI) project (Morgenstern et al., 2017), a follow up model

35   inter-comparison study for ACCMIP. The multi-species assimilation also provides the opportunity to optimize the chemical related species of O_3 and the emission sources of the precursors simultaneously. Further work by Miyazaki, et al. (2017) showed that the surface emission of nitrogen oxides (NO_x) over a 10-year period (2005-2014) has a positive trend in regions include India, China, and the Middle East, but a negative trend over the USA, southern

40   Africa, and western Europe. The global total emission stays almost constant between 2005 (47.9 Tg N yr^{-1}) and 2014 (47.5 Tg N yr^{-1}). Therefore, the O_3 reanalysis data from TCR represents the state-of-the-art for the current knowledge of the global distribution of tropospheric O_3 by combining the complementary information from model and satellite observations for O_3 and its precursors.

In this paper, we demonstrate a method to use the IRK products and the model biases relative to the reanalyzed tropospheric composition (O_3 and H_2O) and atmospheric state (T_s and T_a) to quantitatively attribute the radiative biases of the flux in a suite of CCMI models to these dominant components. The method and IRKs are described in section 2. The models and reanalysis data are introduced in the next section. Section 4 discusses the inter-comparison between models' flux biases, the bias attribution to the dominant components, and the geospatial distribution of the biases. Lastly, conclusion and future directions are summarized in section 5.

2. Instantaneous Radiative kernels (IRKs) for the climate variables

The TOA flux in the 9.6-µm O_3 band (Fig. 1) is defined as

$$F_{TOA} = \int_v \int_0^{2\pi} \int_0^{\frac{\pi}{2}} L_{TOA}(v, \theta, \phi, q) sin(\theta) cos(\theta) \, d\theta d\phi dv \quad (1)$$

where v is the frequency, integrated over the O_3 band from 980 to 1080 cm^{-1}. $L_{TOA}(v, \theta, \phi, q)$ is the upwelling TOA radiance at frequency v, zenith angle θ and azimuth angle ϕ. We assume here that the radiance is symmetric in the azimuthal direction. The outgoing TOA radiances, L_{TOA}, are also a function of the atmospheric state, which is represented by variable 'q', e.g. H_2O, O_3, T_a and etc., that is in turn a function of altitude, z.

The IRKs (Equation 2) represent the sensitivities of the TOA radiative flux in the 9.6-µm O_3 band to the changes in the vertical distribution of an atmospheric variable.

$$\frac{\partial F_{TOA}}{\partial q(z_l)} = \int_v \int_0^{2\pi} \int_0^{\frac{\pi}{2}} \frac{\partial L(v, \theta, \phi, q)}{\partial q(z_l)} sin(\theta) cos(\theta) \, d\theta d\phi dv \quad (2)$$

Where z_l is altitude in discretized level l. When q represents the T_s, z_l becomes a single surface value at $l = 0$.

In this study, we expanded the TES global O_3 IRKs to IRKs with respect to H_2O, T_a, and T_s. The TOA flux sensitivities to H_2O or T_a still refer to the spectral window region in the 9.6-µm O_3 band for the flux. All the kernels are computed with the five-angle Gaussian Integration method (Doniki et al., 2015, Kuai et al., 2017). Figures 2 (a), (c), and (e) show examples of IRK profiles for O_3, H_2O, and T_a for 2006. The TOA flux is most sensitive to each variable at very different vertical levels. The O_3 IRK peaks in the middle and upper troposphere (600 to 200 hPa), a higher level than the peaks in both H_2O and T_a IRKs. The mid and upper tropospheric O_3 near 500 hPa has the largest impact on the TOA flux change (close to 1 mWm^{-2}ppb^{-1} in the tropics). The H_2O IRK peaks near 700 hPa, a little higher than the T_a IRK. The T_a IRK is maximal closest to the surface, suggesting that the O_3 band flux is most sensitive to boundary layer T_a near 900 hPa. The strength of the peaks all decrease with increasing latitude for all the three variables but the

peak altitude does not change significantly except for the H_2O IRKs in the polar region, which peaks at a slightly higher level than in lower latitudes.

In addition, the T_s IRK is greater than zero, which means increases in T_s would increase the outgoing TOA flux. However, the IRKs for the GHGs, i.e. H_2O and O_3, are negative, because the increase in gas concentrations reduces the upwelling flux at TOA due to radiative absorption by the gas.

The global vertical distribution of the zonal averaged kernels for O_3, H_2O, and T_a are also shown below their profile plots in Fig. 2 (b), (d), (f). The sensitivities of the TOA flux to these three variables are strongest in the tropics and decrease with latitude. Furthermore, the IRK for T_s is also shown in Fig. 1 (g) and (h). Unlike the other IRKs, the T_s IRK is not a function of altitude so we show the winter (Dec.-Feb.) and summer (Jun.-Aug.) seasonal average of its global distribution. The flux sensitivities are found to be largest over the major deserts, like Sahara, Middle East, and Australia corresponding to the regions with the highest values of T_s. We also notice that the values of the T_s IRKs in the Inter Tropical Convergence Zone (ITCZ) are much lower than in the subtropics, which suggests that the atmosphere opacity has an impact on the strength of the T_s IRKs.

3. A Method to Attribute the Flux Biases

The flux biases between observations and models under the clear-sky conditions can be described as:

$$\delta F_{TOA}^i \approx \sum_{l \in L} \frac{\partial F_{TOA}^i}{\partial O_3^{i,l}} \delta O_3^{i,l} + \sum_{l \in L} \frac{\partial F_{TOA}^i}{\partial H_2O^{i,l}} \delta H_2O^{i,l} + \sum_{l \in L} \frac{\partial F_{TOA}^i}{\partial T_a^{i,l}} \delta T_a^{i,l} + \sum_{l \in L} \frac{\partial F_{TOA}^i}{\partial T_s^{i,l}} \delta T_s^{i,l} \quad (3)$$

where δF_{TOA}^i, is the total TOA flux bias in the O_3 band at the ith location. The four terms on the right hand side of the equation are the products of the IRKs and the bias in a geophysical quantities (i.e. O_3, H_2O, T_a, and T_s). These biases are then vertically integrated on index, l, over the domain L, which in our case is the troposphere. The summation is the vertical integral from the surface to the tropopause.

Here we assume that the biases due to other physical processes, e.g., surface emissivity or other atmospheric species, have much less influences on the TOA flux variation. For example, the model bias in global emissivity is not accessible, but is believed to be quite small compared to O_3, H_2O, T_a, and T_s. We also assume that the nonlinearity terms are much smaller than these four first order terms.

Following Bowman et al., (2013), the delta terms in Equation (3) are the model bias with respect to the reanalysis data

$$\delta q^{i,l} = q_{mod}^{i,l} - q_{assim}^{i,l} \quad (4)$$

Atmospheric
Chemistry
and Physics
Discussions

where $q_{mod}^{i,l}$ and $q_{assim}^{i,l}$ represents the model and reanalysis O_3, H_2O, T_a, or T_s at the ith location and the lth altitude level respectively.

5   The mean flux bias or the mean bias components from tropospheric uncertainties is calculated from Equations (3) and (4) as

$$\delta F_q^j = \frac{1}{N_j} \sum_{i \in D_j} \sum_{l \in L} w_i \frac{\partial F_{TOA}^i}{\partial q^{i,l}} (q_{mod}^{i,l} - q_{assim}^{i,l}) \qquad (5)$$

10   where w_i is area-weighted for the latitude bands, D_j is a set of observed locations, N_j is the number of locations in the domain of D_j and tropospheric levels L up to the tropopause. We use the chemical tropopause O_3 = 150 ppb (Naik, et al., 2005;Hansen, et al., 2007;Bowman, et al., 2013;Kuai, et al., 2017). The domain of D_j can be zonal bands for the zonal mean or global area for the global mean, respectively. The global mean of the flux bias and its
15   components will be denoted as $\overline{\delta F}$ and $\overline{\delta F_q}$, respectively.

4. Chemistry-Climate Models and the Reanalysis Data

4.1 Models and Simulations
20

We analyze six models from the CCMI study (Table 1) (Morgenstern, et al., 2017;Eyring, et al., 2013). It is a combined activity of the International Global Atmospheric Chemistry (IGAC) and Stratosphere-troposphere Processes And their Role in Climate (SPARC) (Randel, et al., 2004). The CCMI coordinates a number of model experiments that capture the variability and
25   evolution of air quality, tropospheric chemistry, stratospheric O_3, and global climate. This approach builds on the legacy of previous chemistry-climate model inter-comparisons, such as the Chemistry-Climate Model Validation (CCM-Val; SPARC, 2010) (Eyring, et al., 2010) and the ACCMIP;. In this study we use the experiment REF-C1, which is analogous to the REF-B1 experiment of CCMVal-2 (Table S30 in Morgenstern et al., 2017). Using historic forcing and
30   observed sea surface conditions, the models are free-running and simulate the recent past (1960–2010). We didn't choose to use REF-C1SD (specified dynamics) because specified dynamics nudged the wind and temperature of the model to be constrained to the reanalysis data. The long-term climatological biases relative to the reanalysis between the models are minimized. Our study aim to find a correlation between the present day radiative bias and the
35   RF from present day to future by the model predictions. Therefore, we prefer to keep the model differences in simulating longer-term climatology between their free runs.

We note that SOCOL3 and EMAC are both based on different versions of the ECHAM5 climate model. We also added two additional model simulations with AM3 from NOAA and CESM from
40   NCAR. These two simulations are not the specific CCMI experiment run, however, these two models have been used in many studies, and including them in this study would provide more useful information on the TOA flux diversity among the most recent models.

Atmospheric
Chemistry
and Physics
Discussions

Open Access

EGU

4.2 Tropospheric Chemistry Reanalysis (TCR-1) data

5   We computed the biases in the geophysical variables between the model and the reanalysis data. To compute the O_3 bias in models, we used the satellite-based O_3 reanalysis from multi-constituent multi-satellite data assimilation: Tropospheric Chemistry Reanalysis version 1 (TCR-1) (Miyazaki, et al., 2015;Miyazaki and Bowman, 2017) as the best synthesis of the observations. The reanalysis provides comprehensive spatiotemporal and multi-variable evaluation of model
10   performance that compliments direct comparisons against individual measurements, which may suffer from significant sampling bias (Miyazaki and Bowman, 2017).

TCR-1 assimilated multiple species data from multiple satellite products for the period from 2005 to 2017, e.g. combined TES and MLS observations for O_3, integrated OMI, SCIAMACHY and
15   GOME-2 for tropospheric NO_2 column, MOPITT for CO, and MLS for HNO_3. TCR-1 used a global CTM MIROC-Chem (Watanabe, et al., 2011) as a forecast, which includes 92 species and 262 reactions. The model has 2.8° horizontal resolution with 32 vertical layers up to 4 hPa. The data assimilation was based on an ensemble Kalman filter with 32 ensemble members, which was used to simultaneously optimize concentrations and emissions of various species.
20

As summarized by Miyazaki and Bowman (2017), the mean bias in the reanalysis dataset against the WOUDC ozonesonde observations is from −3.9 to −2.9 ppb at the NH high latitudes (55°N −90°N); −0.9 to −0.1 ppb at the NH mid-latitudes (15°N −55°N); and −1.0 to −0.1 ppb at the SH mid-latitudes (55°S −15°S), between 850 and 500 hPa. On average, the bias is about 0.9
25   ppb at the tropics and mid-latitudes between 500 and 200 hPa. These biases are much smaller than biased in the model simulation without data assimilation, demonstrating that the multi-satellite data assimilation provides comprehensive constraints on the entire tropospheric profile of O_3.

30   For the purpose of the consistency, we also use outputs of H_2O, T_a, and T_s from the reanalysis to estimate the model biases. In the reanalysis calculation, meteorological fields simulated by the atmospheric general circulation model MIROC-AGCM (Watanabe et al., 2011) were nudged toward the 6-hourly ERA-Interim meteorological reanalysis (Dee et al., 2011) for zonal wind (τ = 1 day) and temperature (τ = 3 days) to reproduce past meteorological fields while simulating
35   short-term (<six hours) meteorological variations, which were used to drive the CTM, as similarly employed in CCMI C1SD simulations. Thus, the reanalysis dataset provides realistic and comprehensive estimates for both chemical and meteorological fields required for the TOA flux evaluations.

40   ## 5. Results

5.1 The latitudinal distribution of the TOA flux bias

Atmospheric
Chemistry
and Physics
Discussions

Figure 3 shows the latitudinal distribution of the zonal and annual mean of the TOA flux bias from each model relative to the reanalysis. The largest divergence between models is located at the tropics where most models underestimate the flux with the exception of CMAM. The low bias in the model ensemble implies the model atmosphere is more opaque than the chemical reanalysis leading to a 132.9 mWm^{-2} outgoing flux reduction on average. The TOA flux in an opaque atmosphere is less sensitive to changes in tropospheric composition than a more transparent one. Under those conditions, the models would underestimate the radiative feedback from composition since the IRKs estimated under an opaque atmosphere will be weaker than those under a realistic atmosphere, which would be more transparent.

Two models that have significantly larger low biases at the equatorial region than other models are SOCOL3 and MRI-ESM1r1. Their global means of the flux bias are more than −200 mWm^{-2} (Table 2). The following analysis will help to understand the source of the bias in the models.

5.2 Flux bias attribution

The total TOA flux bias is caused by biases from atmospheric composition and temperature. In order to determine the primary drivers of these biases, we apply the IRKs to the differences between model and the chemical reanalysis as described in Equation (3). Figure 4 shows the contribution of O_3 (blue), H_2O (green), T_s (red), and T_a (yellow) for each model to the total TOA flux bias (black). The global mean bias is summarized in Table 2.

In general, O_3 and H_2O are the two dominant drivers for most models where the large biases are concentrated in the tropics and subtropics. There are only three models (GEOSCCM, CMAM, and CESM) whose O_3 radiative biases (δF_{O_3} in Table 2) are less than 50 mWm^{-2} and are almost negligible zonally. While the flux bias is better represented in these models it does not follow that they represent more accurately tropospheric O_3 as will be shown in the following section. The other five models (AM3, SOCOL3, EMAC-L47MA, EMAC-L90MA, and MRI-ESM1r1) have significant negative peaks at low latitudes (Fig. 3 and 4), actually resulting from their strong O_3 contributed biases (from 80 to 180 mWm^{-2}, numbers are highlighted in Table 2).

The TOA flux bias from H_2O is the second largest component for most models. Similar to O_3, most models show the fluxes are biased low in the tropics due to the H_2O uncertainties with the exception of CMAM, which has the strongest global mean bias (127.9 mWm^{-2}). Note that, in the reanalysis, no data assimilation (or nudging) was applied for specific humidity. Watanabe et al (2011) demonstrated a dry bias in the lower troposphere and a wet bias in the middle and upper troposphere in MIROC-AGCM, primarily attributable to temperature biases. Nevertheless, the reported H_2O biases can be greatly reduced in the reanalysis, because of the nudging applied for temperature.

The flux bias due to T_a is found to be negligible in all models, which indicates that the T_a is relatively accurate. While the absolute T_s bias has a larger than the T_s impact for most models, it is still less than 25 mWm^{-2} with the exception of CMAM, which is −100.2 mWm^{-2}. Fig. 4 suggests the strong bias due to the T_s in CMAM comes from the two subtropical regions.

Atmospheric
Chemistry
and Physics
Discussions
Open Access
EGU

Interestingly, the positive flux bias due to H_2O (127.9 mWm^{-2}) is compensated by the negative flux bias due to T_s (–100.2 mWm^{-2}) in CMAM leading to the lowest global mean in $\underline{\delta F}$ (42.9 mWm^{-2}). This compensation is also true for AM3 but between a positive H_2O radiative bias

5   (87.7 mWm^{-2}) and negative O_3 radiative bias (-140 mWm^{-2}). This analysis reveals that these two models are both right but for wrong—and opposite--reasons.

However, all the other models have strong negative global mean bias and are mostly driven by the two major components (O_3 and H_2O) and biased low. SOCOL3 and MRI-ESM1r1 are the two

10   models that have the strongest low bias up to –200 mWm^{-2}, which are found both mainly due to their strong O_3 radiative bias (–180 mWm^{-2}). Their O_3 estimates are both biased high in the tropics and subtropics. We will show later that such bias is particularly strong in the upper troposphere.

15   **5.3 Vertically-resolved radiative bias of the O_3, H_2O and T**

The zonal flux biases among the models are both significant and mainly in the tropics. However, those biases are the vertically integrated product of the model profile bias and the IRKs both with their own vertical structures. The vertically-resolved radiative bias can provide more

20   insight into the processes leading to the biases. To further investigate, we expanded flux bias into vertically for O_3, H_2O and T_a (Fig. 5-7) and globally for T_a (Fig. 8). These are computed from Equation 3 before the vertical summation. These figures show that the maximum contribution to the flux bias is a balance between the peak of the IRKs (Fig 1) and the peak of the geophysical quantities' bias (Fig. 9-12). The positive tropical O_3 radiative bias for GEOSCCM, CMAM, and

25   CESM are commonly centered in the mid-troposphere corresponding to the peak of the IRKs (Fig. 5). On the other hand, the primary O_3 flux bias contribution in the tropics for SOCOL3, EMAC-L47MA, EMAC-L90MA, and MRI-ESM1r1 is in the upper troposphere around 200 hPa even though the IRKs are roughly half the peak sensitivity. These strong negative biases exceed 15 mWm^{-2}. The strong tropical H_2O radiative bias collapses to shallower tropical regions below

30   400 hPa and is maximized near 800 hPa for most models exceeding 50 mWm^{-2} (Fig. 6). CMAM has the unique and strongest net positive bias of above 50 mWm^{-2} centered lower and close to 900 hPa. While most models flux bias is centered near 800 hPa, particularly, GEOSCCM, AM3, and CESM show a more vertically uniform—and opposing—flux bias. Figure 7 indicates that tropical T_a radiative bias is largely negligible for vertical layers above 600 hPa as a consequence

35   of the rapid decrease in sensitivity of the T_a IRKs. The maximum bias is in the lower troposphere between 900 hPa to surface. CMAM and CESM both show the strongest positive bias exceeding 10 mWm^{-2} over most of the tropics. However, CESM has a compensating negative bias from 700-800 hPa that leads to a mean global bias of only 6.4 mWm^{-2} (Table 2), whereas, CMAM has a positive bias throughout leading to an atmospheric T_a radiative bias of 22.5 mWm^{-2}, the

40   largest of the models studied here. Surprisingly, the model ensemble T_s turns out to be the 2nd largest contributor to the total bias (Table 2) instead of H_2O, driven primarily by 3 models: CMAM, CESM, and GEOSCCM as shown in Fig. 8. CMAM shows a negative bias that covers all of Africa exceeding 500 mWm^{-2} and Asia centered over India. Consequently, CMAM has the largest total bias (–100.2 ± 93.3 mWm^{-2}). CESM and GEOSCCM T_s radiative biases, on the other

hand, are centered at high latitudes in the Western Hemisphere over the Eastern US and Canada exceeding 300 mWm^{-2}.

The vertically and spatially concentrated radiative biases provide clues as to what processes are the most important for the total flux bias. These processes drive the distribution of the constituents, which we will discuss more in detail in the next sections.

5.4 The Spatial Source of TOA Flux Bias

The source of the attributed flux biases can be traced back to their spatial origins, which can provide more insight into the underlying processes and the differences between the models.

5.4.1 O$_3$ bias

Figure 9 shows a similar vertically resolved zonal averaged distribution of O$_3$ biases between the model and the chemical reanalysis as in Fig. 5. Three models (GEOSCCM, CMAM, and CESM) have the weakest globally averaged O$_3$ radiative bias reported in Table 2 (−33.5 mWm^{-2}, −7.3 mWm^{-2}, and 3.3 mWm^{-2}). These three models also have the lowest O$_3$ bias in tropical troposphere on average (−1.1 ppb, −1.3 ppb, and 3.0 ppb reported in Table 3) and as a consequence have weaker radiative bias in the region with the strongest O$_3$ IRK globally (0.9 mWm^{-2}, 1.4 mWm^{-2}, and 2.1 mWm^{-2} reported in Table 4). On the other hand, the O$_3$ bias is greater than 7 ppb for all the other models and results in a large O$_3$ radiative bias in tropics, especially SOCOL3 (13.4 ppb in tropical O$_3$ bias and -9.2 mWm^{-2} see Table 3 and Table 4) and MRI-ESM1r1 (13.7 ppb and −10 mWm^{-2}).

GEOSCCM, CMAM, and CESM also commonly have a vertically compensated pattern in the tropics that biased high in the upper troposphere while biased low in the middle and lower troposphere (Fig. 9). Their O$_3$ low biases in the middle troposphere are approximately 5 to 10 ppb, where the peak of the IRK centered, but the high biases in the upper troposphere are about 5 ppb. Such a high-low pattern leads to compensation during the vertical integration through the troposphere into the radiative effect at the top of the atmosphere. The corresponding vertical resolved O$_3$ radiative bias for these three models in Fig. 5 shows the consistent tropical vertical distribution but in an opposite sign since the O$_3$ IRK is negative. In contrast, the other five models have vertically systematic biases high in the tropical O$_3$ and the biases increase from the middle troposphere to the upper troposphere. Especially, SOCOL3 and MRI-ESM1r1 strongly overestimate O$_3$ by more than 20 ppb in a wide region of tropical upper troposphere. The O$_3$ radiative biases in this region remain significantly high, stronger than −15 mWm^{-2}, making these two models to have the highest O$_3$ radiative biases in the global and annual mean (both about −183 mWm^{-2}).

The systematic bias in the entire tropical tropospheric O$_3$ and strong overestimation of upper troposphere in SOCOL3 and MRI-ESM1r1 could be caused by several reasons. For example, the transport from the lower stratosphere could be too high. Alternatively, precursor emissions of

tropospheric O_3 could also be too high. The analysis with the spatially explicit biases provides important clues to implicate the specific processes that individual modeling groups can investigate.

5   The GEOSCCM has been used to study the tropospheric O_3 response to variations in the El Nino-Southern Oscillation (ENSO) where they compared the model to satellite observations (Oman, et al., 2011;2013). These regular comparisons may have led to the improved simulation of tropospheric O_3 profiles and consequently lower vertical O_3 bias.

10   The finding that SOCOL3 and MRI-EMS1r1 both have strong overestimates in the tropical upper troposphere is also understandable. SOCOL3 is the third generation of the coupled chemistry-climate model (CCM) SOCOL (modeling tools for studies of SOlar Climate Ozone Links). Several steps have been taken to improve the SOCOL model simulation of O_3. Stenke et al., 2013 first attempted to reduce the O_3 bias in their middle-atmosphere by updating their middle-
15   atmosphere general circulation with an advanced advection scheme. Revell, et al. (2015) revealed that ozone precursor emissions are the biggest players that control the global-mean change in tropospheric ozone. In a parallel study, Revell, et al., 2018 developed an updated version of "SOCOL3.0", "SOCOL3.1", to reduce the tropospheric ozone bias. By improving the treatment of ozone sink processes, the tropospheric column ozone bias in "SOCOLv3.1" is
20   reduced up to 8 DU, mostly due to the inclusion of N_2O_5 hydrolysis on tropospheric aerosols. We expect that the future similar analysis with the SOCOL3.1 could show a reduced flux bias for this model.

    Meanwhile the strong tropical upper tropospheric O_3 bias in MRI-EMS1r1 is believed to be
25   related to the large lightning NO_x emissions and the weak tropical convective updraft in the model. The model fails to bring enough low O_3 air from the surface to the upper troposphere in the tropics or overestimates the mixing of stratospheric ozone-rich air, which would cause the biases in O_3 and therefore introduces the strong low bias in tropospheric O_3 radiative effect.

30   In summary, the potential reasons for the prevalence of O_3 radiative bias in tropical mid and upper troposphere in the models could be due to following facts: (1) the tropical O_3 IRK is strongest in this region (Fig. 2); (2) the largest O_3 bias in the models also centered in the same place (e.g. SOCOL3 and MRI-EMS1r1, Fig. 9); 3) the systematic bias throughout the tropical troposphere, when propagate into the TOA flux, causes an accumulated bias in the radiative
35   effect.

5.4.2 H₂O bias

40

H_2O turns out to be the primary contributor for three models (GEOSCCM, CMAM, and CESM) since their O_3 radiative bias is small. It is also the second dominant driver after O_3 in the other five models. Different from O_3, H_2O IRKs in Fig. 2 show the strongest sensitivity to the tropical lower troposphere centered at 800 hPa, where H_2O is most concentrated globally. We found

the model biases in H_2O are strongest in the tropical lower troposphere. It explains why the strongest radiative bias from H_2O is also located in the tropical region near 800 hPa in all models as shown in Fig. 6. Figure 10 and Table 3 further help to indicate that H_2O is biased low only in two models, AM3 (–586.5 ppm) and CMAM (–506.6 ppm). We note that H_2O IRKs are also negative as O_3. Therefore, these two models have the unique overestimates in H_2O radiative bias at low latitudes (see Fig. 4) while all the other models are predominantly biased high in tropical H_2O concentrations, which result in the negative radiative biases.

5.4.3 T_a bias

We found the T_a radiative biases in these model ensembles are all negligible. There are two reasons. One is that the T_a biases are small overall (less than 2 K) even at the tropical lower troposphere (below 1 K on average in Table 3). The other reason is that the compensation in the vertical integration helps to reduce the radiative bias at the top of atmosphere.

Figure 11 shows that the model biases in T_a range within ±2 K for all the models because the current chemistry-climate models have been well-developed to simulate the global atmospheric T_a fields relative to reanalysis. The region with strongest sensitivity, identified by the T_a IRKs (Fig. 2), is the tropical lower troposphere (the region within $\pm30°$ and below 800 hPa). The T_a biases in the tropics shift between positive and negative vertically in most models except CMAM, which is relatively constant (Fig. 11). Such oscillation around the observed profile leads to vertical compensation in the air T_a radiative bias. Therefore, the flux bias from T_a is a small component compared to the radiative bias from O_3 and H_2O. Figure 4 suggests the only model that has a small tropical peak in the T_a radiative component is CMAM, which has the strongest T_a radiative bias (22.5 ± 40.5 mWm^{-2} in Table 2) among all the models. Figure 11 shows that this model has a deep region with strong bias of about 2 K at tropical and also persistently overestimated T_a vertically. Figure 7 further suggests the strong radiative bias in CMAM mainly comes from tropical lower troposphere (>10 mWm^{-2} below 800 hPa). While the other models have vertical compensation in the tropics (less than 0.5 K bias on average, see Table 3) and therefore are less biased in TOA flux (less than 1 mWm^{-2} in Table 4). The two EMAC models both have strong biases at southern high latitude but still have weak radiative effect at this region (see Fig. 7) due to much weaker T_a IRK at high latitudes.

5.4.4 T_s bias

The global distribution of the T_a biases indicates that the biases in Sea Surface Temperature (SST) are smaller than the biases in land T_s for all the models (Fig. 12) because the CCMI experiment (REF-C1) selected in this study used the observed SST. CMAM is the model that has the strongest T_s radiative bias (-100.2 ±93.3 mWm^{-2} in Table 2) which peak in both sub-tropical regions (Fig. 4). These large negative biases are due to the strong underestimates of the T_s over the major deserts, e.g., Sahara, Middle East and Australia (Fig. 12). In other words, the real deserts' surface is hotter than the model's prediction. Meanwhile, the T_s IRKs at the subtropical desert region are also strongest globally since the TOA flux is more sensitive to T_a when the atmosphere is transparent, which is due to the downdraft of the Hadley cell control the region

Atmospheric
Chemistry
and Physics

Discussions

(Kuai et al., 2017). The downwelling airflow results in less precipitation and less cloud as well as higher T_s during summer over the desert surface. All these facts cause the CMAM have the largest T_s radiative bias compare to all the other models.

5   In contrast, two EMAC models and MRI-ESM1r1 also have strong high bias in T_s at Siberia (> 4 K in Fig. 12) but the radiative bias is much less significant compared with the Middle East in CMAM in Fig. 8. The T_s IRKs are weaker during the winter season at high latitudes than the low latitudes if the T_s is low (Fig. 2). However, the IRKs at the subtropical desert region stay strong during winter. Therefore, the annual mean of the T_s radiative bias is much weaker at Siberia in
10   two EMAC models and MRI-ESM1r1 than the Middle East region in CMAM. Consequently, the global annual means of the T_a radiative biases for two EMAC models and MRI-ESM1r1 are small although the large biases in T_s are found in their Siberia region.

6. Correlation to the broadband OLR

15

The analysis up to this point has been limited to the 9.6 micron band. We posed the question as to whether biases in this band could provide any insight into biases in the entire OLR band. To that end, we found an anti-correlation (R = − 0.6) between the global mean of the O_3 band flux biases and the clear sky broadband OLR calculated internally by the models as shown in Fig. 13
20   (a). The CMAM OLR is inconsistent with the ensemble (more than 2 Wm^{-2} higher than all the other models) and therefore it is excluded in the correlation. Interestingly, a very similar regression line and anti-correlation coefficient (R = − 0.6) are found between the O_3 radiative bias and the broadband OLR (Fig. 13 b). The similar regression line indicates that the O_3 radiative bias dominates the 9.6-micron TOA flux distribution, which is confirmed by the
25   attribution analysis that O_3 radiative bias is the largest term in five of eight models. The anti-correlation suggests a radiative compensation between the 9.6-micron band and the other parts of the OLR assuming a constant globally integrated OLR at TOA. More interestingly, a strong correlation (R = 0.9) is found between T_s radiative bias and broadband OLR (Fig. 13 c) because the T_s affects the entire baseline of the outgoing radiance and its radiative effect plays
30   a same role in the O_3 band as in the entire OLR. However, there is no significant correlation found between T_a radiative bias and OLR likely because there's no coherent bias in T_a radiative effect between the O_3 band and in the entire OLR. There is neither a correlation between the H_2O radiative bias and broadband OLR. H_2O absorption is ubiquitous in the OLR. Consequently, biases in the 9.6 micron band do not drive the magnitude of the overall H_2O absorption in spite
35   of the H_2O biases.

7. Conclusions

We have demonstrated a new method to quantitatively attribute the biases in O_3 band TOA flux
40   from chemistry-climate model ensembles to O_3, H_2O, T_a, and T_s radiative components using observationally-constrained IRKs. The study also provides the first vertically and globally resolved view of the radiative bias for each component. An IRK depicts the sensitivity of TOA fluxes to the vertical distribution of the geophysical quantities, such as O_3, H_2O, T_a, and T_s. While the products of 9.6-μm O_3 band IRK for O_3, H_2O, T_a, and T_s have been developed with the

satellite observations by Aura TES, the record could be extended by MetOP-IASI and SNPP-CrIS Fourier Transform spectrometer (FTS) measurements. We compute the model biases against reanalysis data for four key variables: O_3, H_2O, T_a, and T_s. Especially for O_3 biases, the newly developed TCR-1 O_3 assimilation data (Miyazaki et al., 2015; Miyazaki and Bowman 2017) are,

5   for the first time, used as the state-of-the-art benchmark for tropospheric O_3 in models.

O_3 abundance is found to be the dominant driver for the ensemble flux bias. Tropical tropospheric O_3 is too high for most models and accounts for about 70% of the flux bias (Table 2). The second driver in the model ensemble becomes the T_s instead of H_2O because the T_s

10   radiative components are commonly biased low in the model ensemble while the H_2O radiative biases between models are biased randomly in both directions with large diversity. For individual models, however, H_2O is the second most important driver, a larger component than T_s, for many cases, such as AM3, SOCOL3, MRI-ESM1r1.

15   In addition to knowing that the tropospheric O_3 and H_2O are overestimated, and the surface is too cold, the study also tells us the geolocations, in latitudes and altitudes, of the deviations in these geophysical quantities that propagate into the flux bias.

The largest spread of the flux bias between the models is found in the tropics. The principal

20   contributors governing each model are different and controlled by different processes over different regions. The flux biases in five of the eight models (AM3, SOCOL3, EMAC-L47MA, EMAC-L90MA, and MRI-ESM1r1) are primary driven by too much O_3 in tropical middle and upper troposphere. H_2O is a big driver in five models (AM3, SOCOL3, GEOSCCM, CMAM, and CESM). T_s is an important contributor in CMAM in addition to its H_2O.

25

Although AM3 and CMAM overall have relative lower TOA flux biases globally, we found they are actually right for wrong reasons. In AM3, the dominant positive H_2O radiative bias (87.7 mWm^{-2} in Table 2) happens to be cancelled by the dominant negative O_3 component (–140 mWm^{-2}). While in CMAM, the large positive H_2O component (127.9 mWm^{-2}) is mostly be

30   composite by T_s radiative bias (–100.2 mWm^{-2}). The two relatively young models among the model ensembles, SOCOL3 and MRI-ESM1r1, have large potential to be improved for their fluxes by reducing their strong negative radiative biases from both tropical upper tropospheric O_3 and tropical lower tropospheric H_2O.

35   On average, the model ensemble underestimates the flux by about 132.98 mWm^{-2} due to overestimated tropical tropospheric O_3 and H_2O. The underestimate of the TOA flux implies the model atmosphere is too opaque. In a more opaque atmosphere, the change in flux will be weaker for the same change in tropospheric O_3 because the sensitivity (i.e., IRKs) is weaker. With such feedback, the O_3 RF, the changes in O_3 GHG effect from pre-industrial to present day,

40   would likely be underestimated. The opacity of the atmosphere is controlled by climate processes, such as the hydrological cycle, that is showed can indirectly affect the O_3 GHG effect and RF, as discussed in Kuai et al., (2017).

The spatially explicit and process-focused differences could be used as a basis for emergent constraints (Bowman et al, 2013). New techniques such as hierarchical emergent constraints (HEC) can harness this spatial information so that specific processes affecting O_3 RF can be identified (Bowman, et al., 2018). Moreover, if this correlation exists between the TOA flux bias and the O_3 RF, then the similar issue could be found in the RF of other GHGs, such as CO_2 and CH_4. That is a subject of future research.

Finally, although the chemical reanalysis dataset provides comprehensive information on model radiative biases, we need understand its performance. For instance, further improvements are still needed for lower tropospheric O_3 (Miyazaki and Bowman 2017). Ingesting more datasets and applying a bias correction procedure would be useful to improve reanalysis accuracy. The lower tropospheric O_3 analysis would be benefited with the recently developed satellite retrievals with high sensitivity to the lower troposphere (Fu, et al., 2018) and the optimization of additional precursor emissions.

Author contributions

Acknowledgement

References:

Aghedo, A., Bowman, K., Worden, H., Kulawik, S., Shindell, D., Lamarque, J.-F., Faluvegi, G., Parrington, M., Jones, D., and Rast, S.: The vertical distribution of ozone instantaneous radiative forcing from satellite and chemistry climate models, Journal of Geophysical Research: Atmospheres, 116, 2011.

5   Bowman, K. W., Shindell, D. T., Worden, H., Lamarque, J.-F., Young, P., Stevenson, D., Qu, Z., delaTorre, M., Bergmann, D., and Cameron-Smith, P.: Evaluation of ACCMIP outgoing longwave radiation from tropospheric ozone using TES satellite observations, Atmospheric Chemistry and Physics, 13, 4057-4072, doi:10.5194/acp-13-4057-2013, 2013.

Bowman, K. W., Cressie, N., Qu, X., and Hall, A.: A hierarchical statistical framework for
10   emergent constraints: application to snow-albedo feedback, Geophysical Research Letters, 2018.

Doniki, S., Hurtmans, D., Clarisse, L., Clerbaux, C., Worden, H., Bowman, K., and Coheur, P.-F.: Instantaneous longwave radiative impact of ozone: an application on IASI/MetOp observations, Atmospheric Chemistry and Physics, 15, 12971-12987, 2015.

15   Eyring, V., Shepherd, T., and Waugh, D.: SPARC report on the evaluation of chemistry-climate models, 2010.

Eyring, V., Lamarque, J.-F., Hess, P., Arfeuille, F., Bowman, K., Chipperfiel, M. P., Duncan, B., Fiore, A., Gettelman, A., and Giorgetta, M. A.: Overview of IGAC/SPARC Chemistry-Climate Model Initiative (CCMI) community simulations in support of upcoming ozone and climate
20   assessments, Sparc Newsletter, 40, 48-66, 2013.

Fu, D., Kulawik, S. S., Miyazaki, K., Bowman, K. W., Worden, J. R., Eldering, A., Livesey, N. J., Teixeira, J., Irion, F. W., and Herman, R. L.: Retrievals of tropospheric ozone profiles from the synergism of AIRS and OMI: methodology and validation, Atmospheric Measurement Techniques, 11, 5587-5605, 2018.

25   Gaudel, A., Cooper, O., Ancellet, G., Barret, B., Boynard, A., Burrows, J., Clerbaux, C., Coheur, P.-F., Cuesta, J., and Cuevas Agulló, E.: Tropospheric Ozone Assessment Report: Present-day distribution and trends of tropospheric ozone relevant to climate and global atmospheric chemistry model evaluation, 2018.

Hansen, J., Sato, M., Kharecha, P., Russell, G., Lea, D. W., and Siddall, M.: Climate change and
30   trace gases, Philosophical Transactions of the Royal Society of London A: Mathematical, Physical and Engineering Sciences, 365, 1925-1954, 2007.

Harries, J. E., Brindley, H. E., Sagoo, P. J., and Bantges, R. J.: Increases in greenhouse forcing inferred from the outgoing longwave radiation spectra of the Earth in 1970 and 1997, Nature, 410, 355, 2001.

35   Kuai, L., Bowman, K. W., Worden, H. M., Herman, R. L., and Kulawik, S. S.: Hydrological controls on the tropospheric ozone greenhouse gas effect, Elem Sci Anth, 5, 2017.

Lamarque, J., Shindell, D. T., Josse, B., Young, P., Cionni, I., Eyring, V., Bergmann, D., Cameron-Smith, P., Collins, W. J., and Doherty, R.: The Atmospheric Chemistry and Climate Model Intercomparison Project (ACCMIP): overview and description of models, simulations and
40   climate diagnostics, Geoscientific Model Development, 6, 179-206, 2013.

Miyazaki, K., Eskes, H., and Sudo, K.: A tropospheric chemistry reanalysis for the years 2005–2012 based on an assimilation of OMI, MLS, TES, and MOPITT satellite data, Atmospheric Chemistry and Physics, 15, 8315-8348, 2015.

Miyazaki, K., and Bowman, K.: Evaluation of ACCMIP ozone simulations and ozonesonde sampling biases using a satellite-based multi-constituent chemical reanalysis, Atmospheric Chemistry & Physics, 17, 2017.

Miyazaki, K., Eskes, H., Sudo, K., Boersma, K. F., Bowman, K., and Kanaya, Y.: Decadal changes in global surface NOx emissions from multi-constituent satellite data assimilation, Atmos. Chem. Phys, 17, 807-837, 2017.

Morgenstern, O., Hegglin, M., Rozanov, E., O'Connor, F. M., Abraham, N. L., Akiyoshi, H., Archibald, A., Bekki, S., Butchart, N., and Chipperfield, M. P.: Review of the global models used within phase 1 of the Chemistry-Climate Model Initiative (CCMI), Geoscientific Model Development, 10, 639-671, 2017.

Myhre, G., Shindell, D., Bréon, F., Collins, W., Fuglestvedt, J., Huang, J., Koch, D., Lamarque, J., Lee, D., and Mendoza, B.: Anthropogenic and natural radiative forcing, Climate change, 423, 2013.

Naik, V., Mauzerall, D., Horowitz, L., Schwarzkopf, M. D., Ramaswamy, V., and Oppenheimer, M.: Net radiative forcing due to changes in regional emissions of tropospheric ozone precursors, Journal of Geophysical Research: Atmospheres, 110, 2005.

Oman, L., Ziemke, J., Douglass, A., Waugh, D., Lang, C., Rodriguez, J., and Nielsen, J.: The response of tropical tropospheric ozone to ENSO, Geophysical Research Letters, 38, 2011.

Oman, L. D., Douglass, A. R., Ziemke, J. R., Rodriguez, J. M., Waugh, D. W., and Nielsen, J. E.: The ozone response to ENSO in Aura satellite measurements and a chemistry-climate simulation, Journal of Geophysical Research: Atmospheres, 118, 965-976, 2013.

Randel, W., Udelhofen, P., Fleming, E., Geller, M., Gelman, M., Hamilton, K., Karoly, D., Ortland, D., Pawson, S., and Swinbank, R.: The SPARC intercomparison of middle-atmosphere climatologies, Journal of climate, 17, 986-1003, 2004.

Revell, L., Tummon, F., Stenke, A., Sukhodolov, T., Coulon, A., Rozanov, E., Garny, H., Grewe, V., and Peter, T.: Drivers of the tropospheric ozone budget throughout the 21st century under the medium-high climate scenario RCP 6.0, Atmospheric Chemistry and Physics, 15, 5887-5902, 2015.

Revell, L. E., Stenke, A., Tummon, F., Feinberg, A., Rozanov, E., Peter, T., Abraham, N. L., Akiyoshi, H., Archibald, A. T., and Butchart, N.: Tropospheric ozone in CCMI models and Gaussian process emulation to understand biases in the SOCOLv3 chemistry–climate model, Atmospheric Chemistry and Physics, 18, 16155-16172, 2018.

Rothman, L., Gamache, R., Goldman, A., Brown, L., Toth, R., Pickett, H., Poynter, R., Flaud, J.-M., Camy-Peyret, C., and Barbe, A.: The HITRAN database: 1986 edition, Applied Optics, 26, 4058-4097, 1987.

Stevenson, D., Young, P., Naik, V., Lamarque, J.-F., Shindell, D. T., Voulgarakis, A., Skeie, R. B., Dalsoren, S. B., Myhre, G., and Berntsen, T. K.: Tropospheric ozone changes, radiative forcing and attribution to emissions in the Atmospheric Chemistry and Climate Model Intercomparison Project (ACCMIP), Atmospheric Chemistry and Physics, 13, 3063-3085, 2013.

Watanabe, S., Hajima, T., Sudo, K., Nagashima, T., Takemura, T., Okajima, H., Nozawa, T., Kawase, H., Abe, M., and Yokohata, T.: MIROC-ESM 2010: Model description and basic results of CMIP5-20c3m experiments, Geoscientific Model Development, 4, 845, 2011.

Worden, H., Bowman, K., Kulawik, S., and Aghedo, A.: Sensitivity of outgoing longwave radiative flux to the global vertical distribution of ozone characterized by instantaneous radiative kernels from Aura-TES, Journal of Geophysical Research: Atmospheres, 116, 2011.

Young, P. J., Naik, V., Fiore, A. M., Gaudel, A., Guo, J., Lin, M., Neu, J., Parrish, D., Reider, H., and Schnell, J.: Tropospheric Ozone Assessment Report: Assessment of global-scale model performance for global and regional ozone distributions, variability, and trends, Elementa: Science of the Anthropocene, 2017.

5

10

15
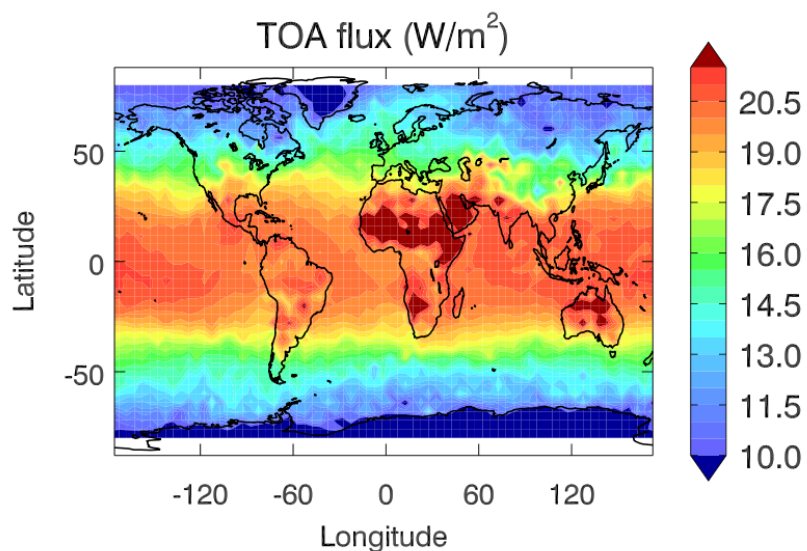
Figure 1. The clear sky TES observed TOA flux at 9.6-μm O_3 band, annually averaged in 2006.

20
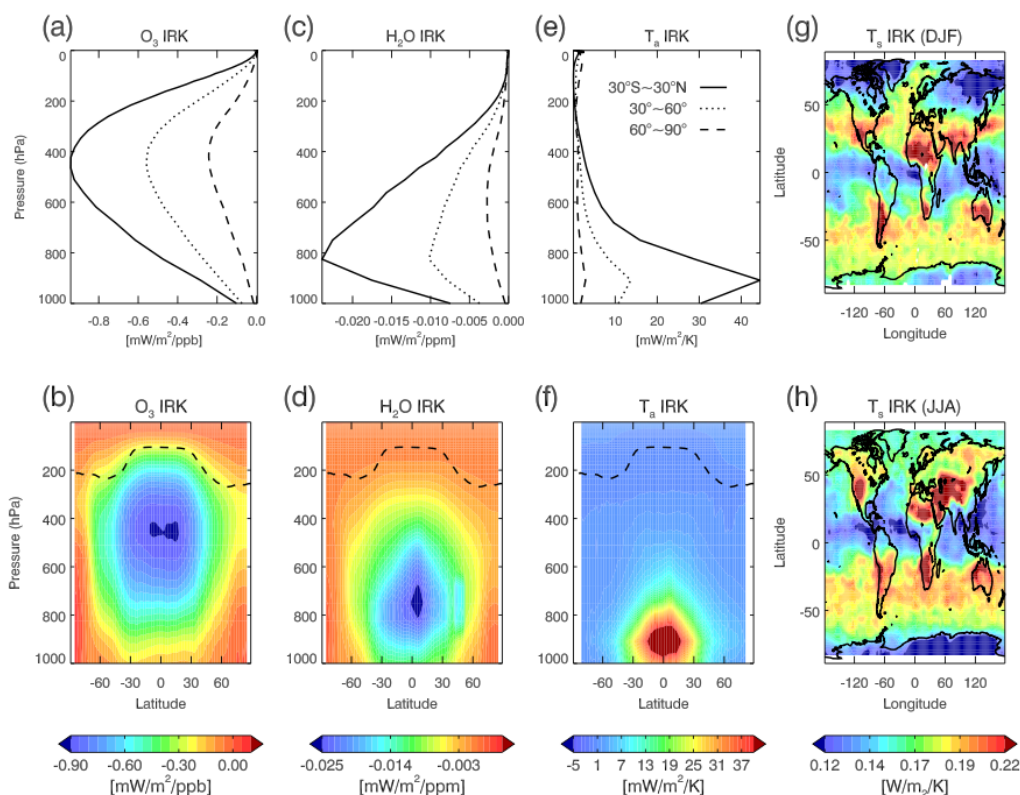
Figure 2. TES 2006 IRK for four primary components (O_3, H_2O, T_a, and T_s). The first top three panels, (a), (c), and (e), are IRK of latitudinal band averages in the tropics (30°S~30°N), mid-latitudes of both hemispheres (30°~60°), and high-latitudes of both hemispheres (60°~90°). The figures below them are the pole-to-pole vertical distribution of the zonally averaged IRK. The global distribution of IRK for T_s is plotted for winter season (December to February) in (g) and summer season (June to August) in (h).
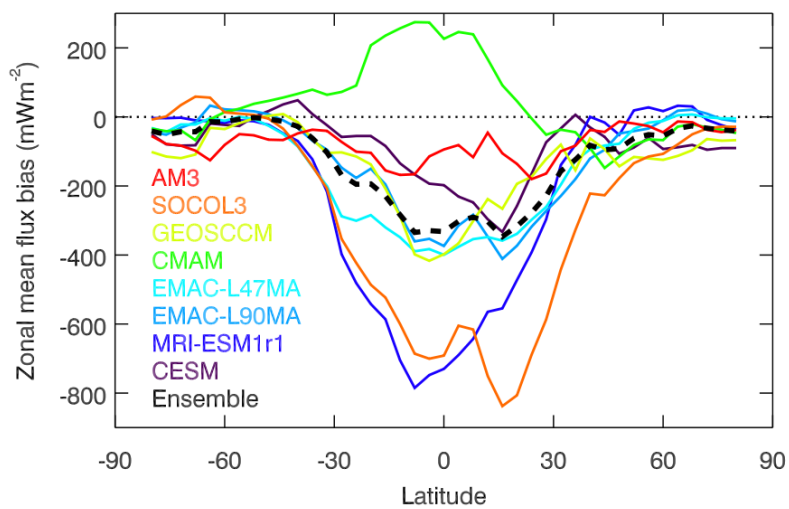
Figure 3. The latitudinal distribution of the zonal flux bias (model – reanalysis) with latitude weight.

5
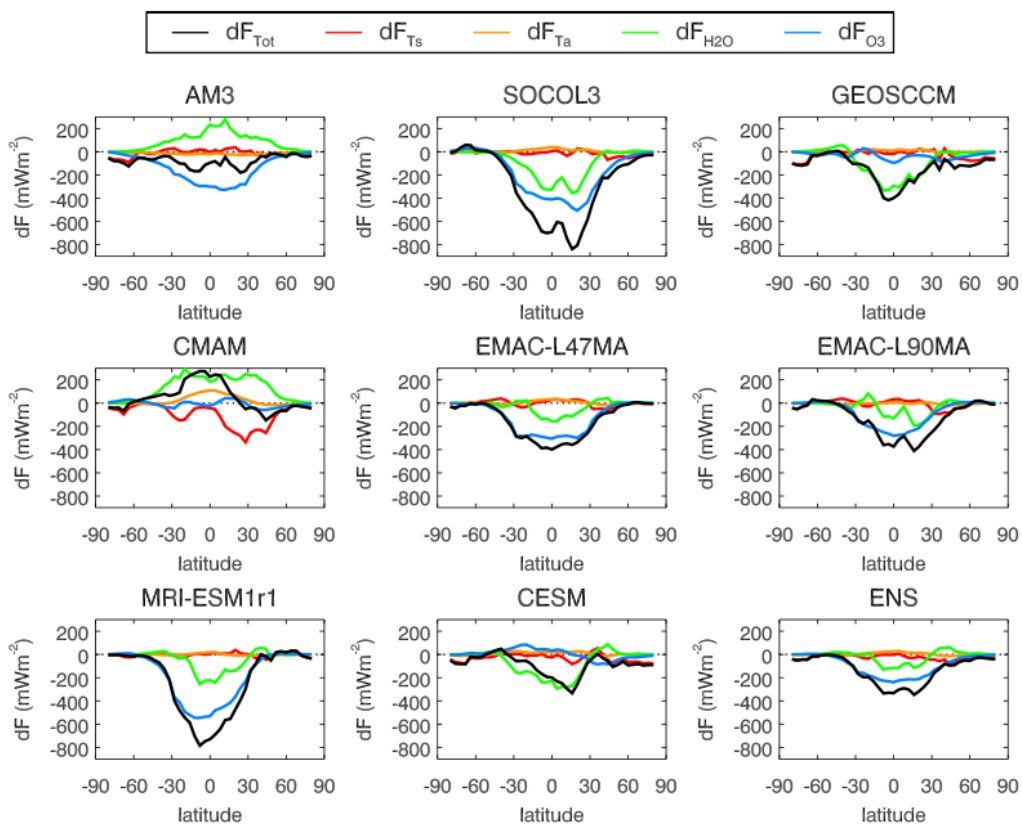
Figure 4. The attribution of the total TOA flux bias for each model to four dominant components and their latitudinal distribution.

5
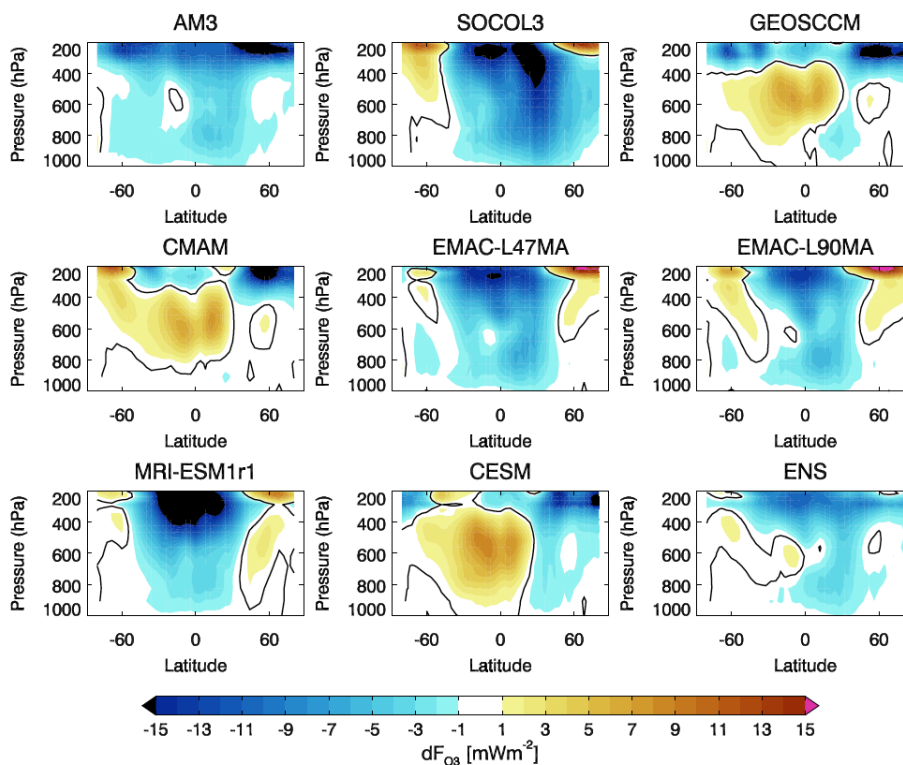
Figure 5. Vertical resolved O₃ radiative bias.
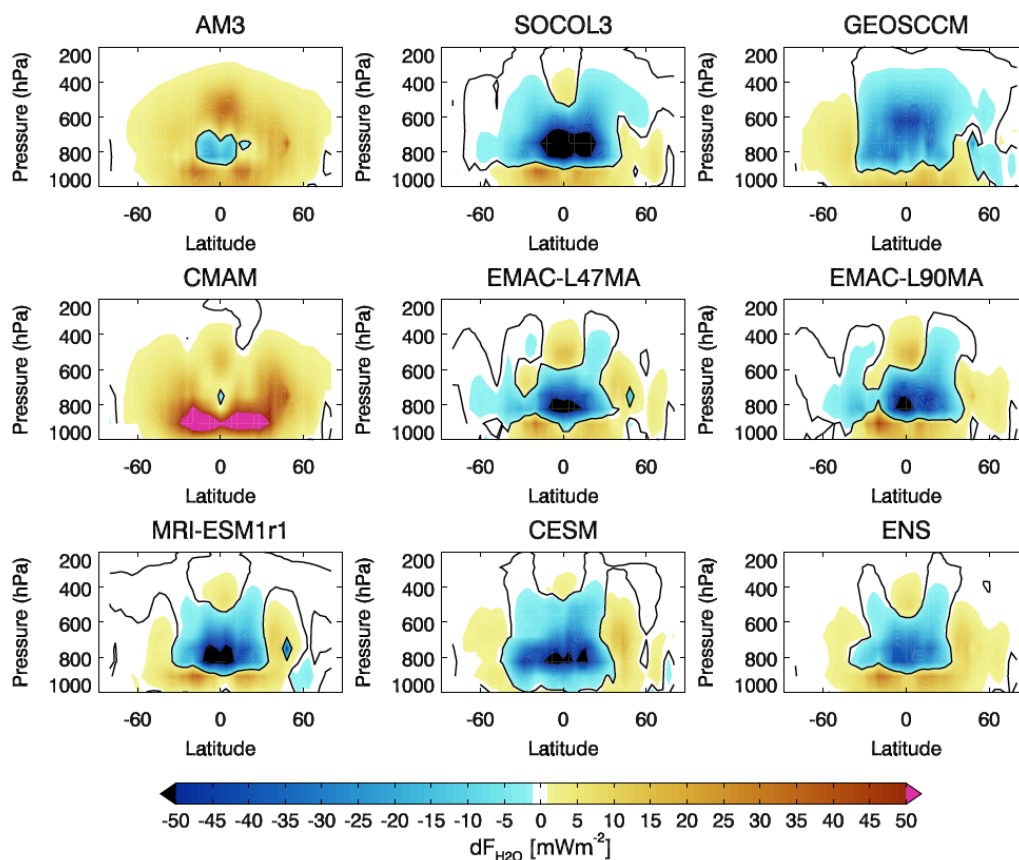
Figure 6. Vertical resolved H_2O radiative bias.
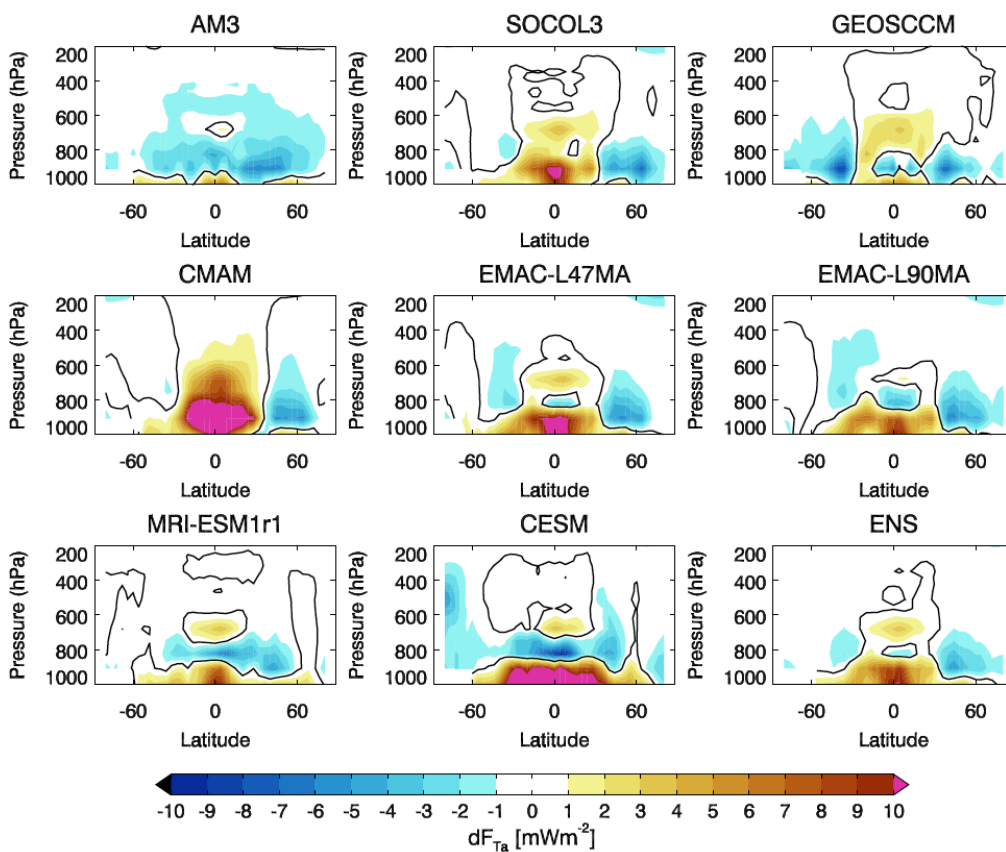
Figure 7. Vertical resolved T_a radiative bias.
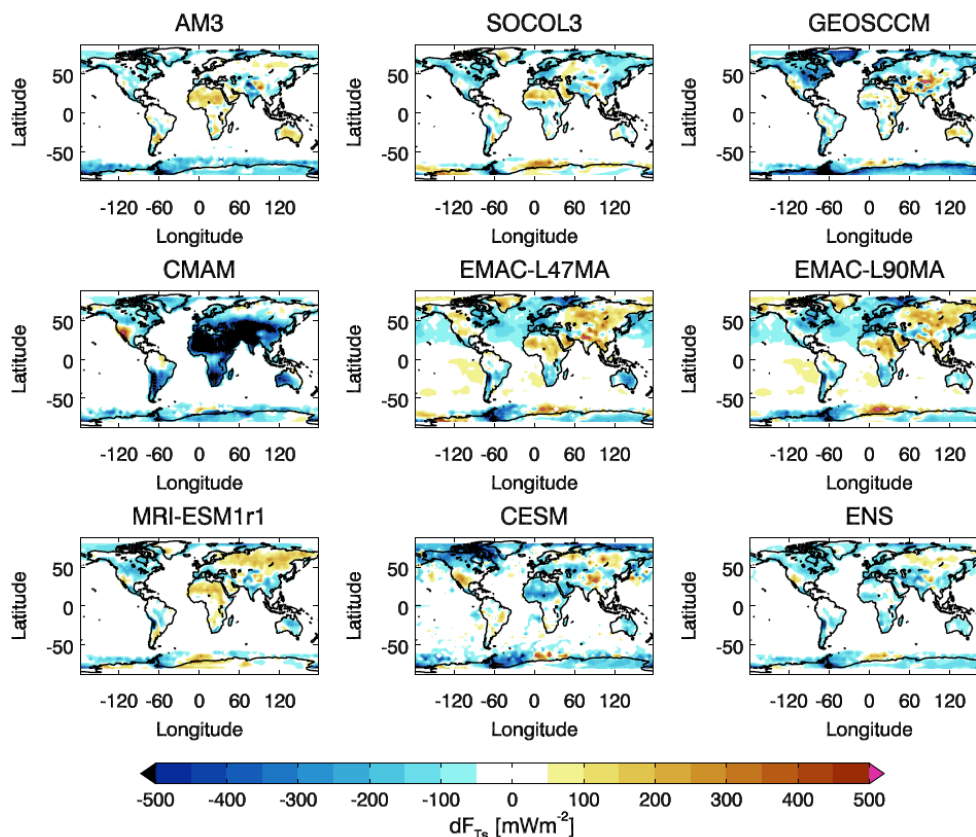
Figure 8. Global distribution of the T_s radiative bias.
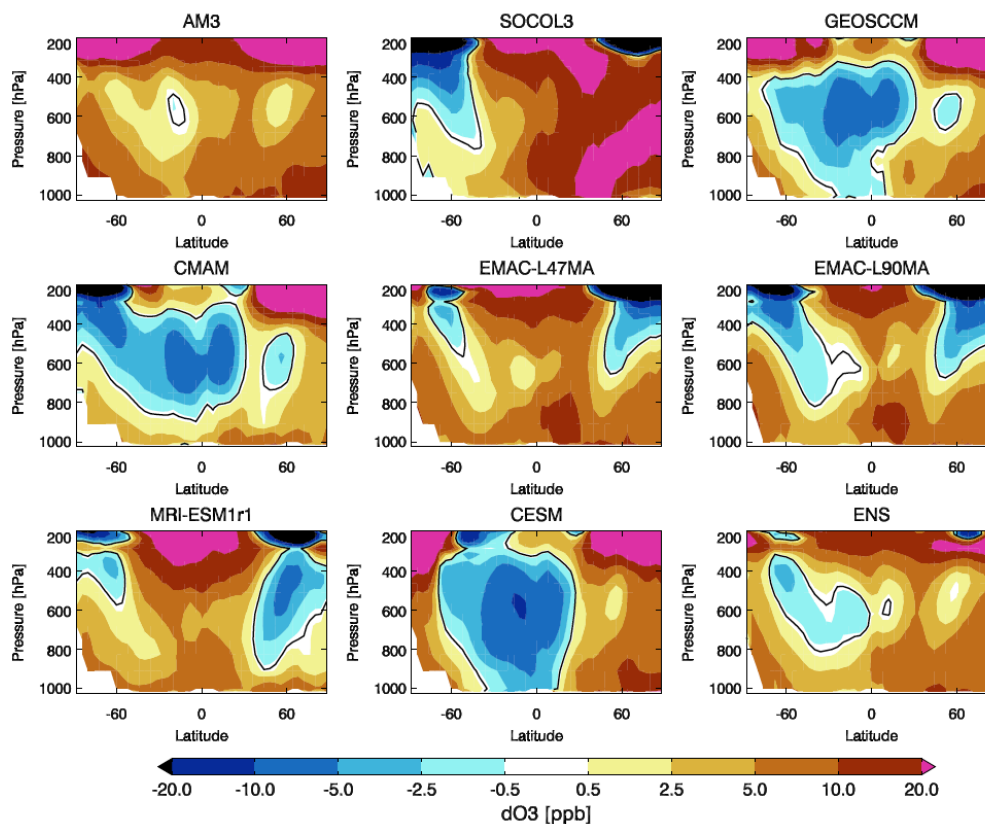
Figure 9. The zonal averaged vertical-latitudinal distribution of O_3 model biases to the TCR-1 O_3 assimilation data. The zero line is plotted in a black line.

5
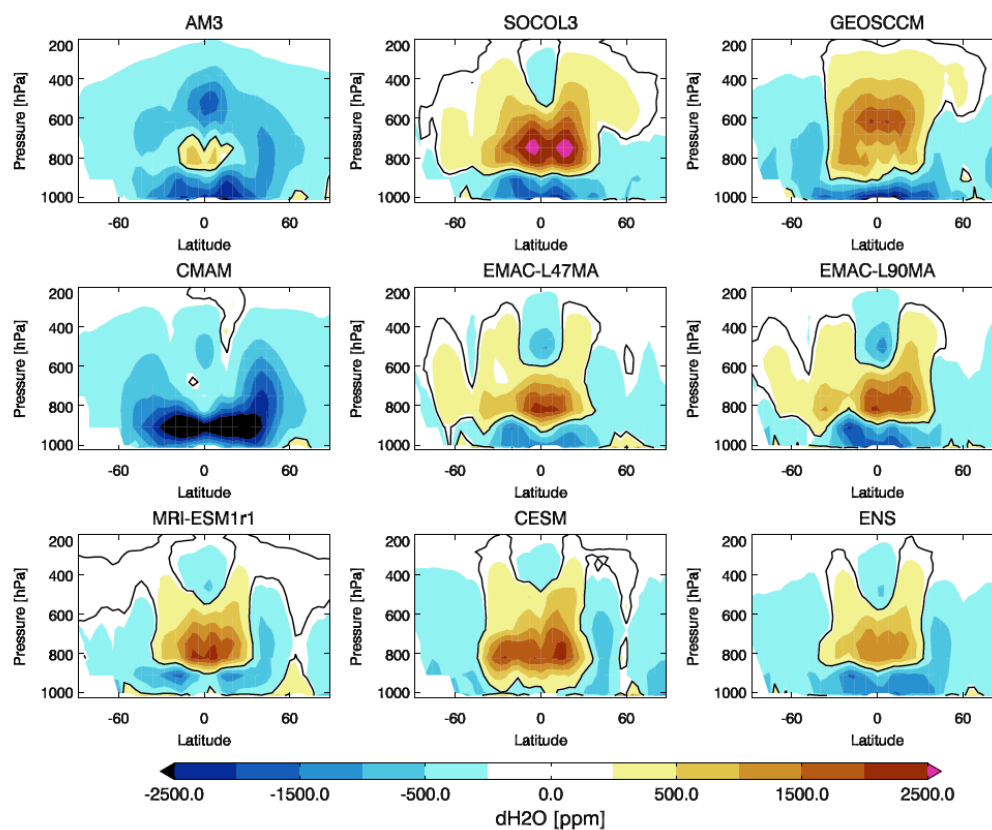
Figure 10. The zonal averaged vertical-latitudinal distribution of H_2O biases (model to the ERA reanalysis data).
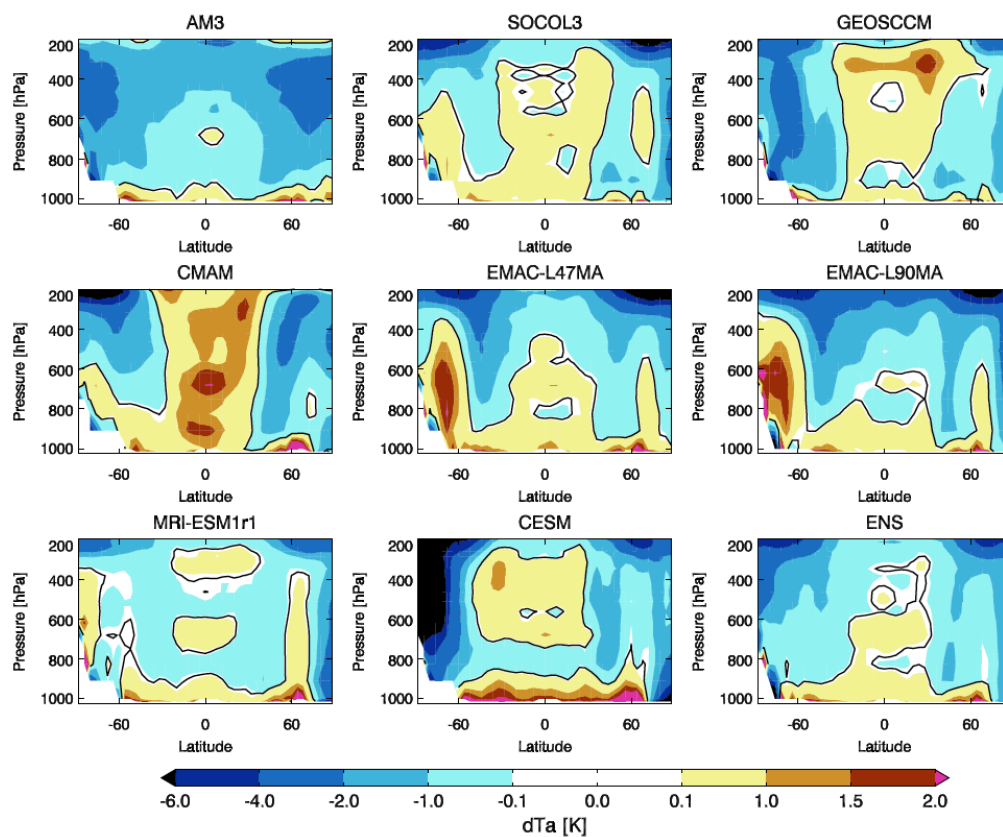
Figure 11. The zonal averaged vertical-latitudinal distribution of T_a biases from models to the reanalysis data

5
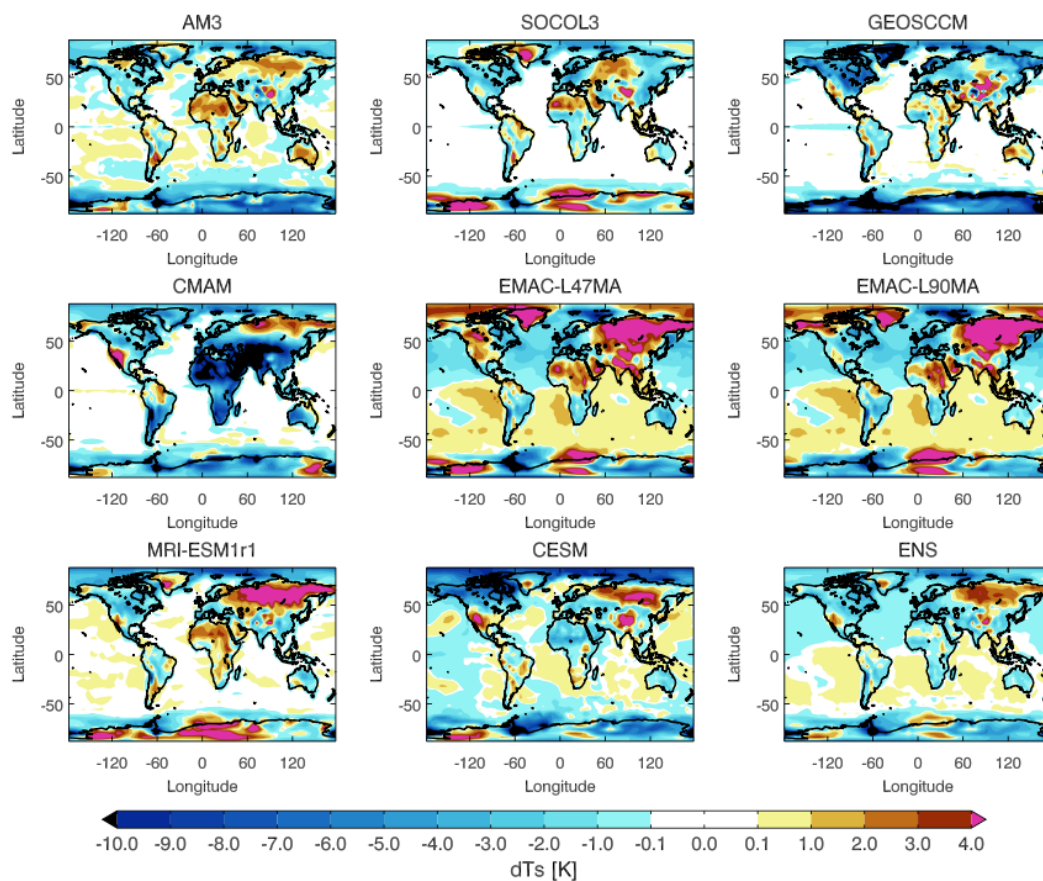
Figure 12. The global distribution of T_a biases from models to the reanalysis data
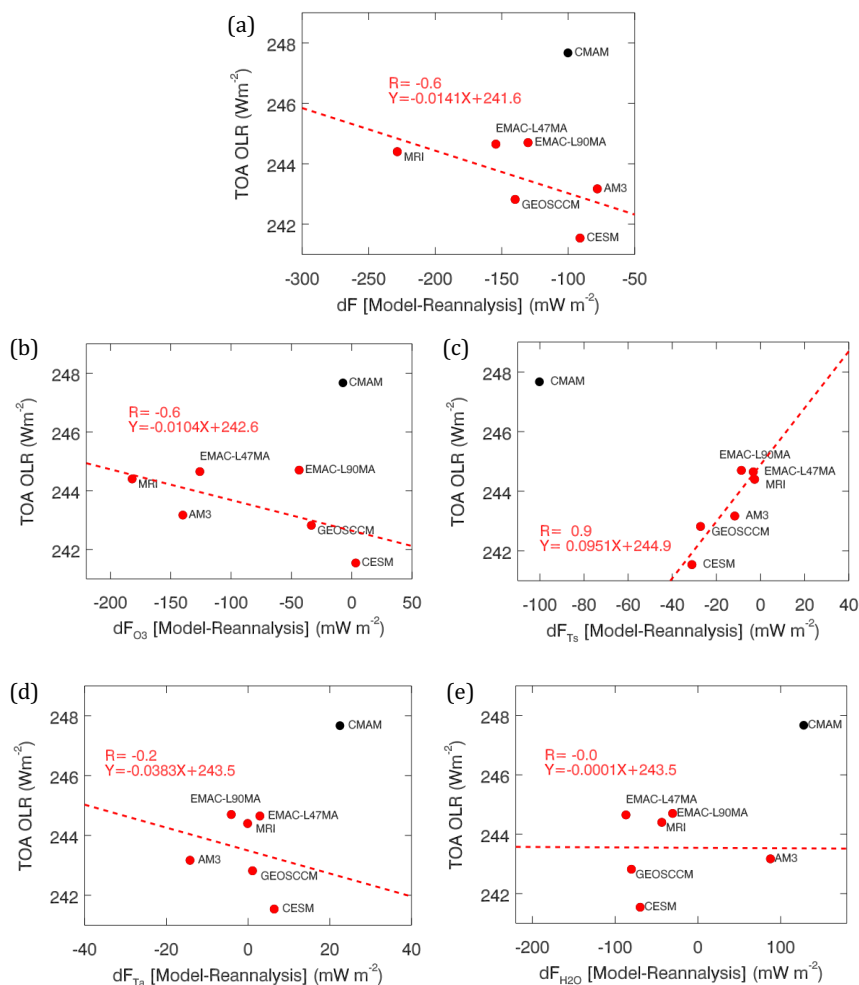
Figure 13. The correlation of the ozone band TOA flux biases to the model calculated broadband OLR (a) and the correlation of the attributed radiative components relate to the broadband OLR (b – e).

Atmospheric
Chemistry
and Physics
Discussions
Open Access
EGU

Table 1. The information of the chemistry-climate models and their experiment simulations

	Model	Institutes	CCMI runs		
1	CMAM	CCCma, Environment and Climate Change Canada	REF-C1	r1i1p1	v1
2	SOCOL3	ETH-Zurich, PMOD/WRC	REF-C1	r1i1p1	v1
3	GEOSCCM	NASA/GSFC	REF-C1	r1i1p1	v1
4	EMAC-L47MA	DLR-IPA,KIT-IMK-ASF,KIT-SCC-SLC,	REF-C1	r1i1p1	v1
5	EMAC-L90MA	FZJ-IEK-7,FUB, UMZ-IPA,MPIC, CYI	REF-C1	r1i1p1	v1
6	MRI-ESM1r1	MRI	REF-C1	r1i1p1	v1
7	AM3	NOAA GFDL	-	-	-
8	CESM	NCAR	-	-	-
	ERA-Interim, TCR-1	Reanalysis	-	-	-

5

10   Table 2 shows that the global mean of the flux bias (mWm^{-2}) and the dominant components due to tropospheric O_3, H_2O, T_a, and T_s. The numbers in parenthesis are the standard deviation of the zonal distribution. For the ensemble, the standard deviation is computed from the variation between the models. The highlighted red numbers are the extreme values for the large biases. Two green numbers highlight the models have relative small global and annual
15   averaged TOA flux bias.

Models	$\overline{\delta F}$	$\overline{\delta F_{T_s}}$	$\overline{\delta F_{T_a}}$	$\overline{\delta F_{H_2O}}$	$\overline{\delta F_{O_3}}$
AM3	−78.1 (46.2)	−11.7 (30.0)	−14.2 (7.8)	87.7 (76.4)	−140 (117.1)
SOCOL3	−283.6 (290.0)	−11.6 (22.3)	5.9 (13.9)	−94.5 (124.6)	−183.5 (187.5)
GEOSCCM	−139.9 (112.0)	−27.2(38.5)	1.1 (12.0)	−80.3 (120.9)	−33.5 (28.0)
CMAM	42.9 (118.5)	−100.2 (93.3)	22.5 (40.5)	127.9 (100.7)	−7.3 (28.8)
EMAC-L47MA	−154.4 (150.0)	−3.3 (27.3)	2.9 (14.8)	−28 (56.1)	−125.9 (128.2)
EMAC-L90MA	−130.2 (142.7)	−8.7 (36.0)	−4.1 (6.6)	−30.5 (63.0)	−86.9 (108.7)
MRI-ESM1r1	−228.5 (281.8)	−2.7 (17.9)	−0.1 (6.8)	−43.6(86.6)	−182 (213.7)
CESM	−91.1 (89.0)	−31.1 (33.9)	6.4 (13.9)	−69.7 (113.0)	3.3 (43.8)
Ensemble	**−132.9 (98)**	**−24.6 (32)**	**2.6 (10)**	**−16.4 (81)**	**−94.5 (75)**

5

Table 3. Models' bias in the tropical troposphere
between 25°S and 25°N, and below 200 hPa.

Models	$\overline{\delta O_3}$ (ppb)	$\overline{\delta H_2O}$ (ppm)	$\overline{\delta T_a}$ (K)
AM3	7.4 (5.0)	−586.5 (669.9)	−1.0 (0.8)
SOCOL3	13.4 (6.8)	330.3 (1067.3)	0.1 (0.4)
GEOSCCM	−1.1(4.3)	−506.6 (949.1)	0.5 (0.5)
CMAM	−1.3 (3.9)	18.1 (949.5)	1.0 (0.4)
EMAC-L47MA	10.4 (6.1)	−20.2 (729.1)	−0.2 (0.6)
EMAC-L90MA	8.2 (5.6)	203.1 (845.1)	−0.9 (1.0)
MRI-ESM1r1	13.7 (9.3)	386.9 (679.9)	0.1 (0.4)
CESM	−3.0 (4.4)	22.0 (630.7)	0.3 (0.7)

10

Table 4. Models' flux bias (mWm^{-2}) in the tropic troposphere
between 25°S and 25°N, and below 200 hPa.

Model	$\overline{\delta F_{O_3}}$	$\overline{\delta F_{H_2O}}$	$\overline{\delta F_{T_a}}$
AM3	-4.8(3.7)	6.9(10.5)	-0.7(1.4)
SOCOL3	-9.2(5.3)	-9.1(21.6)	1.0(2.2)
GEOSCCM	1.0 (3.3)	-8.5(14.1)	0.7(1.4)
CMAM	1.4(2.8)	9.1(18.5)	3.1(5.0)
EMAC-L47MA	-7.2(4.8)	-3.2(15.3)	1.0(2.9)
EMAC-L90MA	-5.6(4.2)	-2.7(16.4)	0.2(2.2)
MRI-ESM1r1	-10.0(7.4)	-5.5(16.4)	0.3(2.0)
CESM	2.1(3.4)	-8.3(15.0)	1.3(4.5)
Ensemble	-4.06(4.90)	-2.66(7.02)	0.86(1.1)